



UNIVERSITY OF LEEDS

This is a repository copy of *Morphologies and dynamics of micro-droplet impact onto an idealised scratch*.

White Rose Research Online URL for this paper:
<https://eprints.whiterose.ac.uk/176355/>

Version: Submitted Version

Article:

Al-Ghaithi, KHA, Harlen, OG orcid.org/0000-0002-4593-3547, Kapur, N orcid.org/0000-0003-1041-8390 et al. (1 more author) (2021) Morphologies and dynamics of micro-droplet impact onto an idealised scratch. *Journal of Fluid Mechanics*, 925. A23. ISSN 0022-1120

<https://doi.org/10.1017/jfm.2021.638>

Reuse

See Attached

Takedown

If you consider content in White Rose Research Online to be in breach of UK law, please notify us by emailing eprints@whiterose.ac.uk including the URL of the record and the reason for the withdrawal request.



eprints@whiterose.ac.uk
<https://eprints.whiterose.ac.uk/>

Morphologies and Dynamics of Micro-Droplet Impact onto an Idealised Scratch

Khaled H. A. Al-Ghaithi¹, Oliver G. Harlen,² Nikil Kapur³, and Mark C. T. Wilson^{3†}

¹EPSRC CDT in Fluid Dynamics, University of Leeds, Leeds, LS2 9JT, UK

²School of Mathematics, University of Leeds, Leeds, LS2 9JT, UK

³School of Mechanical Engineering, University of Leeds, Leeds, LS2 9JT, UK

With the continued drive to smaller printed features using inkjet technologies, there is a growing impact of scratches and surface defects on the final print quality. With printed electronics, a growth area of application within inkjet printing, this can cause breaks in the continuity of circuits. Here, a validated, GPU-accelerated, 3D multiphase lattice Boltzmann model is used to elucidate the physics of droplet deposition into scratches of commensurate size to the droplets. For the geometrical class of scratch examined here, seven equilibrium morphologies of the final droplet are identified, highlighting the rich physical behaviour of the system. This is captured in a regime map, on which the influences of Reynolds and Weber numbers and advancing and receding contact angles are illustrated. Modelling droplet deposition dynamics identifies printing failure modes associated with the dimensions of the scratch causing a break in a line, or capillary flow along the scratch causing unintentional connections between printed parallel tracks. Subtle changes to operating parameters also suggest line continuity can be recovered, for example using a subsequent droplet to modify the position of the preceding one. Multiple-droplet simulations of printing along a scratch also show that deliberate scratch-like features on a substrate could be exploited to achieve uniform tracks.

1. Introduction

The impact and coalescence of inkjet droplets on a solid substrate are of paramount importance to several industries including printed electronics, ceramic and tile decoration, and printing biological materials. Inkjet technology in the printed electronics industry has received increasing interest due to the method's potential to reduce the manufacturing costs of some devices (Soltman 2011). Example devices include passive circuit elements, organic transistors, organic light-emitting diodes, sensors, and radio frequency identification tags (Kwon *et al.* 2018; Soltman 2011). Small imperfections in the substrate surface can arise through small variations during manufacturing, or as a result of unintended damage, such as scratching during transportation and/or handling of the substrate. These can pose a challenge for printing continuous tracks to form electrical circuits (Chilton 2012), particularly as the droplet sizes are progressively decreasing in the quest for higher resolutions. Topographical features can also be added to substrates

† Email address for correspondence: m.wilson@leeds.ac.uk

to control the flow of the droplets (Seemann *et al.* 2005; Kant *et al.* 2017). This makes understanding the behaviour of the fluid and the morphologies formed in the presence of such topographical features important.

A significant amount of experimental, computational, and theoretical work has focused on the impact of single and multiple droplets onto smooth or nominally flat rough substrates, making these parts of the problem relatively well studied. The dynamics of a single droplet impacting a solid smooth surface can be classified into three stages. In the first stage, the droplet spreads due to inertia on an air layer which prevents direct contact with the substrate. This air layer is either expelled or trapped in the droplet as a bubble when the droplet eventually makes contact with the substrate; for more detail refer to the review on droplet impact onto solid surfaces by Josserand & Thoroddsen (2016). In the second stage, surface tension causes the droplet to oscillate or relax depending on the degree of viscous dissipation. In the final stage, the droplet spreads under capillary forces reaching an equilibrium that minimises free energy. The three stages were labelled by Rioboo *et al.* (2002) as kinematic and spreading, relaxation, and wetting/equilibrium. Models to predict the equilibrium spreading diameter have been developed (van Dam & Le Clerc 2004) as well as to predict the maximum spreading diameter, such as Pasandideh-Fard *et al.* (1996) and Roisman (2009).

Only a few studies have examined the effect of features on substrates. Bussmann *et al.* (1999) studied the impact of millimetre-sized droplets onto a substrate with a sharp step. They found that a droplet can split due to the presence of a corner. De Jong *et al.* (2015) studied experimentally the impact of similar-sized droplets near closed pits and open-ended pores and their effect on splashing. Most relevant to this study, since we consider micro-droplets, Rashidian *et al.* (2019) developed an analytical model and used lattice Boltzmann method (LBM) simulations to investigate how the presence of a small protrusion can cause the rupture of a droplet's spreading lamella and the effect of impact velocity, wettability and protrusion dimensions on this phenomenon. It is found that the presence of a small protrusion can rupture the lamella of the spreading droplet possibly resulting in a non-continuous coating. Kant *et al.* (2017) studied experimentally the spreading of a micro-droplet on a substrate with a recessed pixel and found that the presence of its side wall can either enhance or hinder spreading depending on the gradient of the topography ahead. They found that topography can be used to restrict small volumes of liquids to a specific region; a droplet spreading with the topography ahead sloping downhill will be pinned. Jackson *et al.* (2019) used LBM simulations to explore the effects of misalignment between droplets and small cavities and the filling of the cavities.

Seemann *et al.* (2005) studied the wetting of micro-structured surfaces using regular grooves separated with ridges. A small liquid volume was deposited using vapour condensation. Two main morphologies were ascertained, namely an overspilling droplet that extends onto the ridges and neighbouring grooves, and extended filaments that run parallel to the grooves. As droplet sizes decrease in size, it is expected that substrate topographical features will have a greater effect on the printed morphology and product quality. There have been no studies of how such minor variations or defects on a substrate change the morphology of an impacting droplet. Therefore, we study the effect of a generic 2-D feature that can be deliberately designed or accidentally caused by scratching. To explore what droplet morphologies form due to the presence of this feature, and the associated dynamics, we use a validated 3-D multiphase lattice Boltzmann method solver described in the next section.

The remainder of this paper is arranged into five sections: we detail the LBM multiphase solver in §2, simulate a droplet printed onto a flat substrate (§3) and validate the

where s_ζ and s_ν determine the bulk and kinematic shear viscosities respectively. s_π and s_q are relaxation rates for non-hydrodynamic moments that can be tuned to ensure the stability of the simulation. The term $S_\alpha(\mathbf{x}, t)$ in equation (2.1) is a source term used here to incorporate inter-molecular forces needed to produce coexistence of liquid and vapour phases. To simulate multiphase flow, Shan & Chen (1993) introduced local attractive interaction forces written in discrete form as,

$$\mathbf{F}(\mathbf{x}, t) = -G\psi(\mathbf{x}, t) \sum_{\alpha} w_{\alpha} \psi(\mathbf{x} + \mathbf{e}_{\alpha} \delta t, t + \delta t) \mathbf{e}_{\alpha}, \quad (2.4)$$

where G is the strength of the interactive force, $\psi(\mathbf{x}, t)$ is the pseudo-potential used to prevent the force from diverging at high densities, and w_{α} are weights that depend on the velocity directions; they are $w_0 = 1/3$, $w_1, \dots, w_6 = 1/6$ and $w_7, \dots, w_{18} = 1/12$. This interaction force is incorporated differently into $S_\alpha(\mathbf{x}, t)$ in the original Shan & Chen (1993) model than in Li *et al.* (2013), where the latter solves the thermodynamic inconsistency in the former. The source term used in this work is that proposed by Li *et al.* (2013), and is detailed in appendix A. This model results in a pressure, $p = c_s^2 \rho + \psi^2 c_s^2 G/2$, supporting two phases, where $c_s = 1/\sqrt{3}$ is the speed of sound of the lattice (Shan & Chen 1993). Yuan & Schaefer (2006) showed that this equation of state, with the choice of $\psi(\mathbf{x}, t) = \rho_0(1 - \exp(-\rho/\rho_0))$ originally proposed by Shan & Chen (1993), is limited in terms of achievable density ratio between the liquid and vapour phases and instead proposed using a different expression for $\psi(\mathbf{x}, t)$,

$$\psi(\mathbf{x}, t) = \sqrt{\frac{2(p - c_s^2 \rho(\mathbf{x}, t))}{c_s^2 G}}. \quad (2.5)$$

This enables using different equations of state for pressure such as the Carnahan-Starling equation of state used in this work,

$$p = \rho RT \frac{1 + b\rho/4 + (b\rho/4)^2 - (b\rho/4)^3}{(1 - b\rho/4)^3} - a\rho^2, \quad (2.6)$$

where $a = 0.49963R^2T_c^2/p_c$ and $b = 0.18727RT_c/p_c$, where T_c and p_c are the critical temperature and pressure respectively, T is temperature, and R is the universal gas constant set to 1. In this study, we use equation (2.6) with $a = 0.05$, $b = 4$ and $T = 0.00472$ which enable a density ratio of $O(1000)$. The macroscopic variables of density, pressure, and velocity are calculated from the moments of the probability density function using the following equations respectively,

$$\rho(\mathbf{x}, t) = \sum_{\alpha} f_{\alpha}(\mathbf{x}, t), \quad (2.7)$$

$$p(\mathbf{x}, t) = c_s^2 \rho(\mathbf{x}, t) + \frac{c_s^2 G}{2} \psi^2(\mathbf{x}, t), \quad (2.8)$$

$$\rho(\mathbf{x}, t) \mathbf{u}(\mathbf{x}, t) = \sum_{\alpha} \mathbf{e}_{\alpha} f_{\alpha}(\mathbf{x}, t) + 0.5\delta t \mathbf{F}, \quad (2.9)$$

while the kinematic viscosity is given by

$$\nu = c_s^2 (s_{\nu}^{-1} - 0.5\delta t). \quad (2.10)$$

2.2. Wetting and contact angle hysteresis boundary condition

Various methods can be used to prescribe a contact angle at a wall boundary, such as introducing an interaction force between the solid and fluid nodes (see for example Li

et al. (2014)) or prescribing a constant density at the wall to achieve a predetermined contact angle (see for example Castrejón-Pita *et al.* (2013)). These methods work well at relatively low density ratios but become unstable at higher values. The prescription of a density at the wall also requires calibration to give a specific contact angle whenever the density ratio or the equation of state is changed (Wilson & Kubiak 2016). An alternative is to use the geometric boundary condition developed by Ding & Spelt (2007), which has been used to simulate inkjet printed droplets at high density ratio without loss of stability, and hence it is used in this study. This condition was originally developed for the volume of fluid method and adopted in the phase field multiphase lattice Boltzmann methods by Conington & Lee (2013) and has been used for the pseudo-potential multiphase models by Zhang *et al.* (2018). A derivation detailed in Appendix A.2 results in the equation

$$\tan\left(\frac{\pi}{2} - \theta\right) = \frac{-\nabla\rho \cdot \mathbf{n}}{|\nabla\rho - (\nabla\rho \cdot \mathbf{n})\mathbf{n}|}, \quad (2.11)$$

where \mathbf{n} is the unit normal to the solid surface and ρ is the density. This can be discretised and used to calculate a density to assign to the solid wall locally to satisfy a given contact angle. The discrete form for our geometry is detailed in Appendix A.2.

Contact angle hysteresis was implemented by calculating the local contact angle using the inverse of equation (2.11). If the value of the local contact angle is lower than the receding contact angle (θ_R) then θ is replaced with θ_R and similarly, if the local contact angle is higher than the advancing contact angle, it is replaced with θ_A . Assigning the density on the wall controls the interaction pseudo-potential in equation (2.5) to satisfy the contact angle θ . In order to capture CAH, the wall lattice sites are initialised with θ in equation (2.11) set to θ_A . This allows the droplet to spread provided that the contact line forms a local contact angle of $\theta \geq \theta_A$. Once a lattice site has been wetted, the value of θ in equation (2.11) is replaced with θ_R for this lattice site. This will stop the droplet from dewetting or the contact line to recede unless the local contact angle at contact line is $\theta \leq \theta_R$. This is implemented by rearranging equation (2.11) for θ and calculating in every time step locally in every wall lattice site. Note that the values of θ assigned at the wall are used to control the interaction force, while the contact line can have any contact angle. The Shan & Chen (1993) model with these additions can capture a range of contact angles, contact angle hysteresis, coalescence and breakup, and contact line dynamics at high density ratio up to 10^3 . A mesh sensitivity study was carried out and is summarised in Appendix A.3.

To enable the extensive parametric study presented in section 4, the code was accelerated using CUDA to run on GPUs. A simulation that would take up to 3 days (of size $256 \times 256 \times 576$ lattice cells) on a single CPU then ran in under two hours. On a 24 core CPU HPC node (Intel Xeon Gold 6138 @ 2GHz) speeds of 5 million lattice update per second (MLUPS) compared with 200 MLUPS on an NVIDIA P100 GPU and 500 MLUPS on an NVIDIA V100 GPU.

3. Droplet deposition on smooth flat surface

To validate the simulation methodology, published experimental measurements of the impact and spreading of droplets on a smooth surface are compared with corresponding simulations in section 3.1. Simulation results are also compared to analytical predictions for equilibrium and maximum spreading diameters of a spreading droplet in section 3.2. In addition to validation, the simulation of a micro-droplet deposition onto a flat surface provides a base-line for comparison with subsequent simulations.

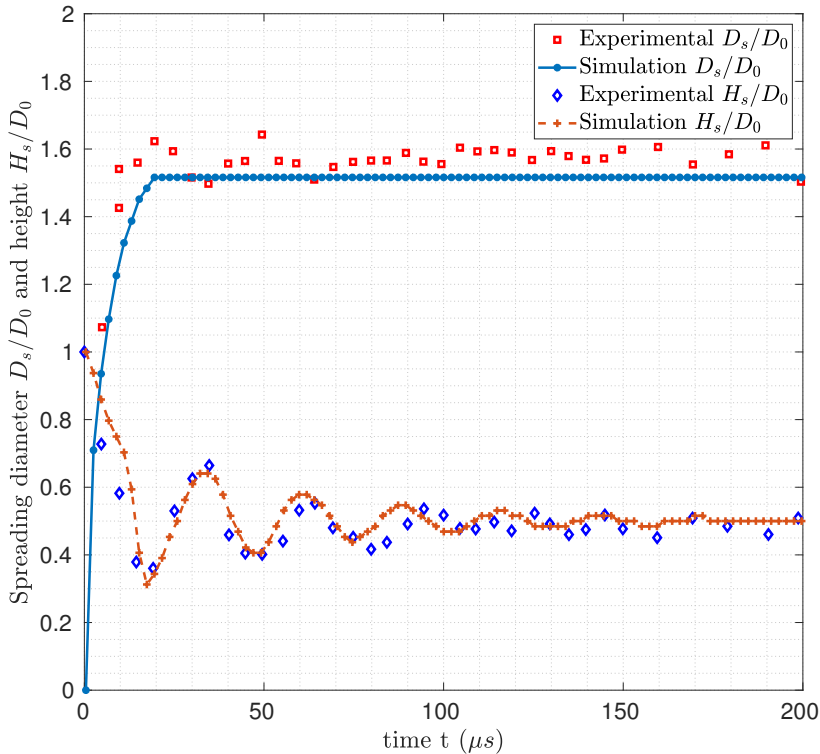


Figure 1: A comparison between the experimental results by Lim *et al.* (2009) and corresponding simulation.

3.1. Validation of simulation against experimental data

For the impact of a single droplet falling onto a smooth solid surface we compare our simulations to experimental data from Lim *et al.* (2009), who examined droplets with in-flight diameter $D_0 = 48.1 \mu\text{m}$ hitting a smooth surface at speed $u = 1.8 \text{ m s}^{-1}$ corresponding to a Reynolds number $Re = uD_0/\nu = 107$, Weber number $We = \rho u^2 D_0/\gamma = 2.59$, and Ohnesorge number $Oh = \sqrt{We}/Re = 0.015$, where γ is the surface tension. The advancing and receding contact angles were reported to be $\theta_A = 91^\circ$ and $\theta_R = 32^\circ$ respectively. The normalised spreading diameter of the droplet D_s/D_0 and height H_s/D_0 were tracked over time. Lim *et al.*'s (2009) data are compared with an equivalent simulation in figure 1. Good agreement can be seen between the simulations and both sets of experimental data; oscillations in height agree well in terms of magnitude and frequency, while the growth and final diameter agrees, with some small variation in experimental data due to experimental noise.

3.2. Comparison with analytical models

Theoretical models have been developed to predict the equilibrium diameter D_{eq} for a given static contact angle θ (in the absence of hysteresis) as well as predicting the maximum spreading diameter. Using conservation of volume, van Dam & Le Clerc (2004) derived an expression for D_{eq} in terms of the in-flight diameter of the droplet D_0 and θ :

$$\frac{D_{eq}}{D_0} = \left(\frac{8}{\tan \frac{\theta}{2} (3 + \tan^2 \frac{\theta}{2})} \right)^{1/3}. \quad (3.1)$$

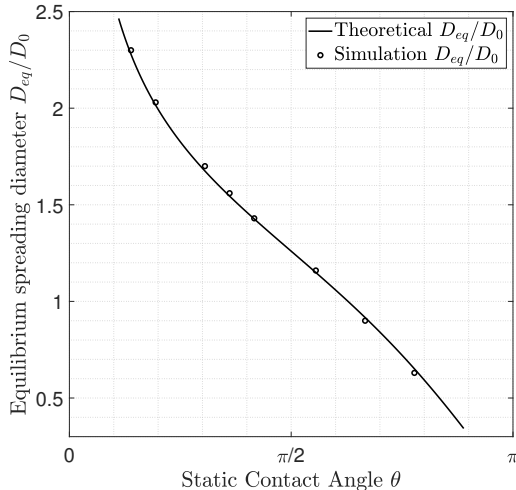


Figure 2: The equilibrium diameter theoretically expected by equation 3.1 compared to that from simulation.

In a recent review, Josserand & Thoroddsen (2016) evaluated various models for predicting the maximum spreading diameter of a droplet, with most models agreeing well with experimental droplet spreading data. An example analytical model is that by Pasandideh-Fard *et al.* (1996):

$$\frac{D_{max}}{D_0} = \sqrt{\frac{We + 12}{3(1 - \cos \theta_A) + 4(We/\sqrt{Re})}}. \quad (3.2)$$

As validation for the simulation methodology, and to provide a baseline simulation for more complex topographies, a typical inkjet droplet impacting a smooth surface was simulated. The droplet was $48.8 \mu\text{m}$ in diameter falling at 3.74 m s^{-1} , with density 1000 kg m^{-3} , surface tension 26 N m^{-1} , and dynamic viscosity $9 \times 10^{-4} \text{ Pa s}$ (i.e. $Re = 204$ and $We = 26$). Several simulations were run without CAH with various static contact angles, and the resulting equilibrium diameters were compared to values predicted by equation 3.1 as shown in figure 2. Very good agreement is seen.

To compare with equation (3.2), a simulation including CAH was conducted, with $\theta_A = 75^\circ$. The receding contact angle was chosen to be $\theta_R = 1^\circ$ in order to achieve the contact line pinning seen in practice with the colloidal inks used in the printed electronics industry (Duineveld 2003). The advancing contact angle was chosen to be less than 90° since this is a condition necessary for printing continuous lines and morphologies (Davis 1980). In this simulation, the droplet impacts the surface and spreads to reach a maximum spreading diameter $D_s = D_{max}$ and does not recede, as shown in figure 3 plotting the time evolution of the spreading diameter D_s . This value of D_{max} agrees with equation 3.2 to within a 2.5% error. The time evolution of the case without CAH is also plotted in the same figure. In that case, the droplet reaches the same D_{max} , but then recedes and oscillates before finally settling at D_{eq} as expected from equation (3.1). Having validated the model with experiments and theoretical predictions, droplet impact on more complex topography is considered in the next section.

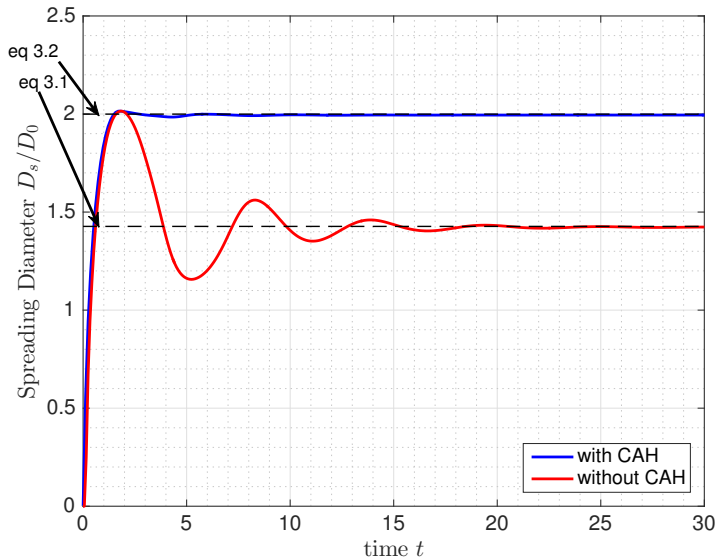


Figure 3: The spreading diameter D_s as a function of time for a single droplet on a smooth surface. These are results from simulations with and without CAH compared to predictions by Pasandideh-Fard *et al.* (1996) and van Dam & Le Clerc (2004): equations 3.2, and 3.1 respectively.

4. Droplet deposition onto an idealised scratch

4.1. Geometry representation

Here, the deposition of a single droplet onto grooves with and without side ridges is studied. These geometries mimic an idealised scratch or a micro-structured surface such as those studied by Seemann *et al.* (2005). The geometry with ridges is illustrated in figure 4 and the second geometry is the same but with the side ridges removed. The groove is continuous with depth from the the substrate surface to scratch bottom d and an additional $0.5d$ above the substrate surface in the case with ridges to represent displaced material. The ridges represent material displaced during scratching and, therefore, have the same volume as the groove. These side ridges can also represent the edge between two neighbouring grooves in micro-structured substrates. The groove and side ridges have the same width, w . The droplet's initial diameter is D_0 . In the parametric study, width w is varied between $0.1D_0 - D_0$ and the depth d between $0.05D_0 - 0.5D_0$. These values were chosen to study the outcomes of micro-droplet impact when the droplets and grooves have commensurate sizes. The range in widths is larger because grooves made by a scratching mechanism tend to be wider than deep (Do *et al.* 2011).

4.2. Printed droplet morphologies

The resulting equilibrium morphologies for the groove with ridges will be considered here and the case without them later in section 4.4. Running the simulations for the various widths and depths until an equilibrium morphology has formed for each simulation, seven distinct morphologies are identified. These are named by considering the shape of the morphology, how it formed (i.e. by inertial spreading or capillary flow), whether or not splitting occurs, and/or the degree to which the droplet imbibes into the surface feature. The seven morphologies are named as quasi-spherical cap, capillary,

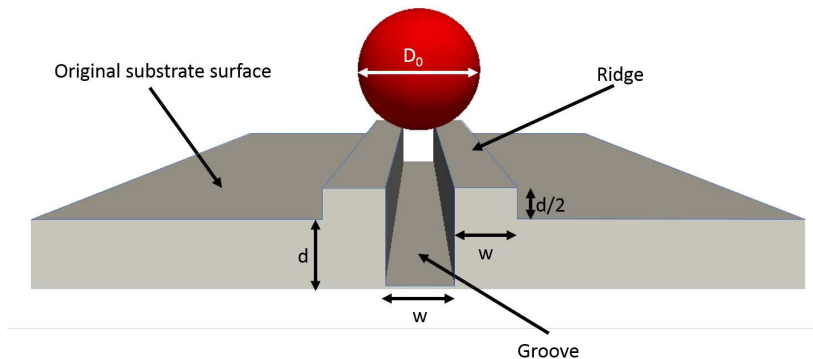


Figure 4: The geometry used to represent an idealised scratch. The groove has width w and so do the side ridges. The groove has a total depth of d from the original substrate surface and an extra $0.5d$ above this; this extra $0.5d$ contribution is omitted for the case without ridges.

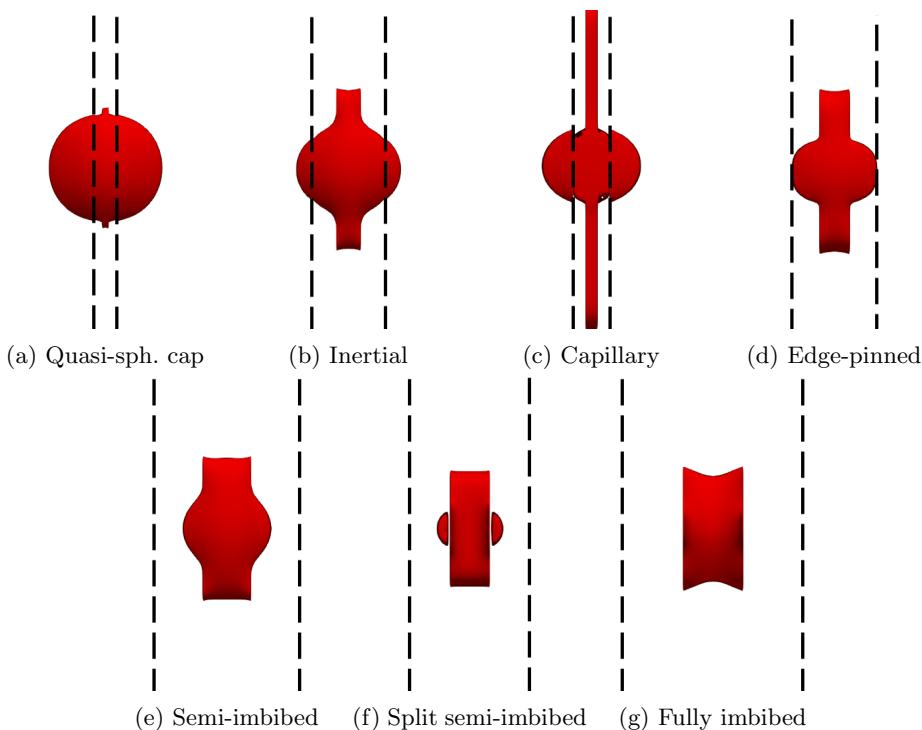
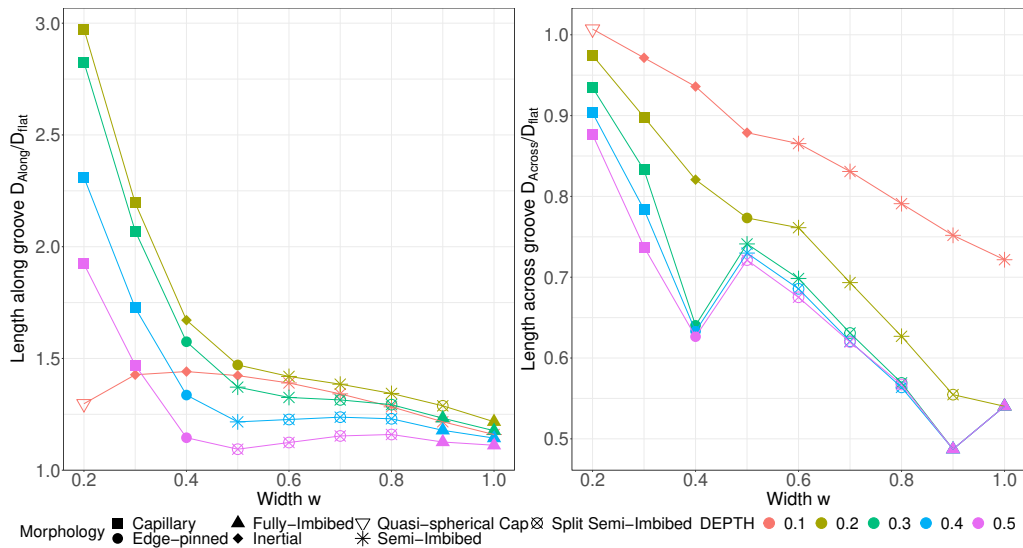
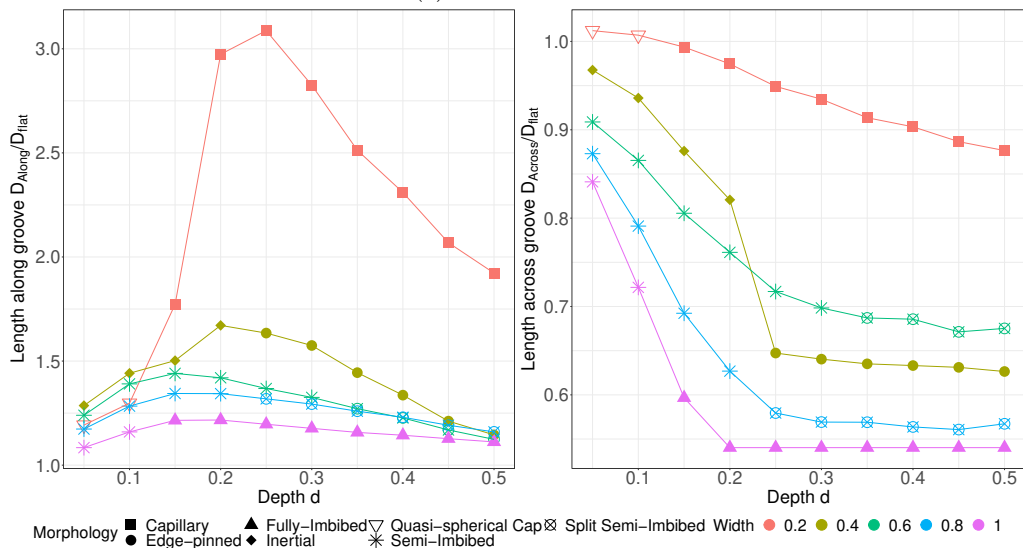


Figure 5: Seven new equilibrium morphologies result from micro-droplet impact onto an idealised scratch. The dashed lines represent the outer edges of the side ridges — see figure 4.

inertial, edge-pinned, quasi-imbibed, split quasi-imbibed and fully imbibed; see figure 5. Top view images for all the groove widths and depths are in table 1, and the diameters of the equilibrium morphologies in the direction along the groove, D_{Along} , and across it, D_{Across} , are plotted as functions of groove depth and width in figure 6. Diameters are



(a) Effect of Width



(b) Effect of Depth

Figure 6: Equilibrium dimensions of the morphologies as a function of (a) depth, and (b) width of the groove with side ridges.

normalised by the spreading diameter of the same droplet depositing on a flat surface D_{flat} . This normalisation assists in finding the deviation from a spherical cap caused by the presence of the groove. For $D_{Along}/D_{flat} > 1$, the morphologies are longer in the direction parallel to the groove. For $D_{Across}/D_{flat} < 1$, morphologies are shorter in this direction than the baseline droplet. The type of morphology occurring for different groove depth and width combinations is summarised in a regime map in figure 7.

For very thin and shallow grooves, there is insignificant deviation from a spherical cap as seen in figure 5a, hence the name “quasi-spherical cap”. A small amount of the

Table 1: Top views of equilibrium morphologies for printing onto a scratch with various widths and depths for $Re = 204$ and $We = 26$. The depths and widths are fractions of the in-flight diameter D_0 .

depth	width									
	0.1	0.2	0.3	0.4	0.5	0.6	0.7	0.8	0.9	1.0
0.05										
0.10										
0.15										
0.20										
0.25										
0.30										
0.35										
0.40										
0.45										
0.50										

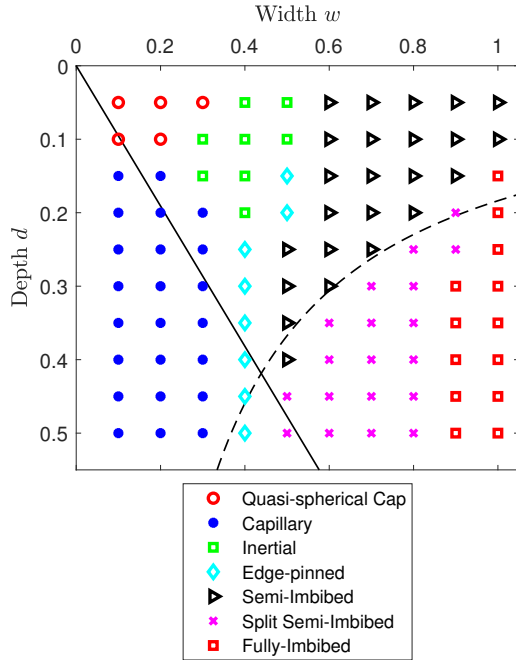


Figure 7: Regime map for morphologies formed by printing a single centred droplet onto a scratched substrate for various depths and widths of scratches for $Re = 204$ and $We = 26$. The solid line is the boundary for capillary flow from equation (4.1), and the dashed line is given by equation (4.2).

droplet imbibes into the groove, so the printed droplet is slightly longer along the scratch, however, there is a negligible effect on D_{Across} as seen in figure 6. Increasing the width of the groove, while keeping the depth very shallow, results in more liquid invading the groove and consequently less spreading across; this causes significant deviation from a spherical cap as seen in figure 5b. This morphology is named “inertial” and is characterised by overspilling the ridges onto the original substrate and the absence of an extremely elongated filament along the scratch seen later in the capillary regime. This inertial morphology was observed by Seemann *et al.* (2005) using condensation into grooves. Within the inertial morphology region, see figure 7, increasing groove width decreases D_{Across} while increasing the groove depth increases D_{Along} and decreases D_{Across} . These trends happen because when the width or depth of the scratch are increased, more fluid penetrates along the scratch before it spreads across it.

When the groove is narrow and deep, long filaments form within the groove, as seen in figure 5c, as a result of capillary action, hence the name “capillary”. The final length of the filaments increases sharply with increasing groove depth, as seen in figure 6b, due to more fluid being allowed to penetrate the scratch and then being stretched by capillary flow. This length reaches a maximum, however, and starts decreasing for deeper grooves because the droplet volume is finite.

In the aforementioned cases, the spreading droplet spills over onto the original substrate (or into neighbouring grooves had they been present). Increasing the groove width enough will result in the contact line of the droplet being pinned on the outer edges of the side

ridges as seen in the “edge-pinned” morphology in figure 5d. This Gibbs pinning of the contact line at the sharp outer edge occurs because the liquid no longer has enough inertia to carry it past the edge, and the very low receding contact angle prevents recession. Hence the Gibbs pinning criterion is satisfied. Similar pinning on rounded edges has been observed by Kant *et al.* (2017). The contact-line pinning results in a sharp decline in the diameter D_{Across} of the morphology as seen in figure 6b due to overspill failure. As depth is increased, D_{Along} decreases and D_{Across} remains constant due to pinning.

The range of widths where the edge-pinned morphology is found is relatively small, and increasing the groove width moves into the “semi-imbibed” regime where the contact line of the spreading droplet stops before reaching the outer edge of the ridges — see figure 5e. At fixed width in the edge-pinned regime, D_{Across} values for various depths collapse to a single point due to pinning at the outer edge, see figure 6a. Increasing the depth further we again reach the semi-imbibed regime. When the groove is sufficiently deep, the part of the droplet that is imbibing into the groove can become separated from the parts that sit on top of the ridges — i.e. the droplet splits along the *inner* edge of the groove. This is identified as a separate morphology, named “split semi-imbibed” and shown in figure 5f, with the corresponding region indicated in the regime map in figure 7. Finally, when the scratches are very wide and deep, the droplet fully imbibes into the scratch, leaving no liquid on the upper horizontal surfaces, see figure 5g.

There are two distinct mechanisms that can result in significant deviation of morphologies from a spherical cap. The first is due to capillary flow forming in the scratch which produces a long filament. This mechanism is dominated by the width of the scratch since capillary flow occurs in sufficiently thin scratches. Yang *et al.* (2011) predict a critical width below which capillary flow will occur for open rectangular channels given by

$$w_c = 2d \cos \theta_A / (1 - \cos \theta_A). \quad (4.1)$$

This is plotted in figure 7 and agrees well with the boundary of the capillary regime identified from simulations. The slight deviation between this condition and simulations is because equation (4.1) assumed an infinite source of fluid and does not capture fore due to the Laplace pressure due to curvature of the droplet. The other mechanism is the imbibition of the majority of the droplet into the scratch, which is expected to occur when the cross-sectional area of the scratch multiplied by the length of spreading along the scratch results in the same volume as the droplet. This corresponds to when $wD_0 \times dD_0 \times D_{Along} = \frac{4}{3}\pi(D_0/2)^3$, i.e. when

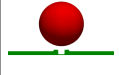
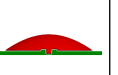
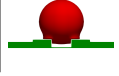
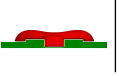
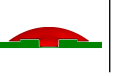
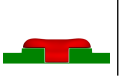
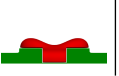
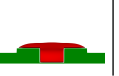
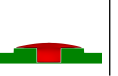
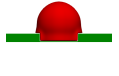
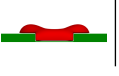
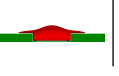
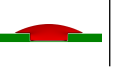
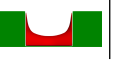
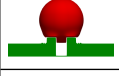
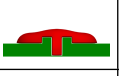
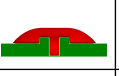
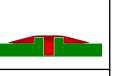
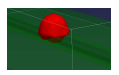
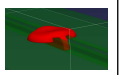
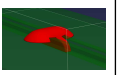
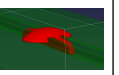
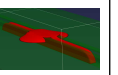
$$w = 0.088\pi/d, \quad (4.2)$$

assuming $D_{Along}=D_{flat} = 1.9D_0$ from figure 3. This is also plotted on the regime map in figure 7 and agrees well with the simulations.

4.3. Droplet spreading dynamics

Having described the equilibrium morphologies, here we discuss further the dynamics that lead to them. As the names of the seven morphologies in figure 5 suggest, two types of flow dominate the spreading dynamics, namely inertial and capillary flow. Front views of the droplet spreading process at different times for the various regimes are shown in table 2, while figure 8 shows the evolution of the dimensions D_{Along} , D_{Across} , and H normalised by the equilibrium diameter D_{flat} and height H_{flat} of a corresponding droplet after impact on a smooth flat surface, i.e. with no scratch. Note that H is measured at the centre of the scratch from the bottom of the scratch to the free surface; it, therefore, includes the depth of the scratch below the original surface. In the quasi-spherical cap regime, the scratch is filled and covered very quickly, the droplet spreads to reach a

Table 2: Snapshots of the different regimes evolving in time measured in milliseconds.

Regime	Time Evolution (ms)					
Quasi-spherical $d = 0.05$ $w = 0.1$	$t = 0$	$t = 0.03$	$t = 0.039$	$t = 0.048$	$t = 0.072$	$t = 0.138$
						
Inertial $d = 0.1$ $w = 0.4$	$t = 0.03$	$t = 0.036$	$t = 0.042$	$t = 0.048$	$t = 0.069$	$t = 0.12$
						
Edge pinned $d = 0.15$ $w = 0.5$	$t = 0$	$t = 0.036$	$t = 0.045$	$t = 0.048$	$t = 0.066$	$t = 0.12$
						
Semi Imbided $d = 0.1$ $w = 0.8$	$t = 0.033$	$t = 0.036$	$t = 0.042$	$t = 0.048$	$t = 0.066$	$t = 0.12$
						
Split Semi Imbided $d = 0.45$ $w = 0.7$	$t = 0.033$	$t = 0.036$	$t = 0.042$	$t = 0.048$	$t = 0.066$	$t = 0.12$
						
Fully Imbided $d = 0.5$ $w = 1$	$t = 0.036$	$t = 0.045$	$t = 0.048$	$t = 0.054$	$t = 0.057$	$t = 0.066$
						
Capillary with 3D view $d = 0.25$ $w = 0.2$	$t = 0.033$	$t = 0.036$	$t = 0.048$	$t = 0.066$	$t = 0.195$	$t = 5.7$
						
						

maximum diameter and then oscillates rapidly, as seen in the H curve in figure 8a, before relaxing more slowly to an equilibrium. The resulting horizontal dimensions D_{Along} and D_{Across} are similar to the corresponding spherical cap formed on a smooth flat surface. However, the slight extension of the droplet along the scratch results in a lower equilibrium height.

In the inertial regime, the droplet touches the side ridges, then penetrates to the bottom surface of the scratch. The liquid spreads on the side ridges and spills over onto the original substrate surface, as seen in the second row of table 2. Figure 8c shows that the droplet spreads along the substrate up to $1.5D_{flat}$ and D_{Across} is reduced compared to D_{flat} . The height again oscillates rapidly then increases gradually as the droplet relaxes to equilibrium. In the edge-pinned regime, the contact line of the droplet reaches the outer edge, but, as noted in §4.2, there is insufficient momentum to carry the free surface past the edge, and the contact line remains pinned as seen in table 2. The centre of the droplet oscillates in height, but rapidly reaches an equilibrium.

In the semi-imbibed morphology, the droplet impacts the bottom of the scratch and spreads along and across and then impacts onto the side ridges. The droplet spreads on the top of the side ridges but the contact line does not reach the outer edges; it becomes pinned somewhere on the top of the ridges because of the very low receding contact angle. In the split-semi-imbibed regime, the droplet impacts the side ridges first, and then penetrates into the scratch, reaching the bottom and spreading along it. As the droplet spreads into the scratch, it splits along the inner edges of the side ridges, leaving separated almost flat droplets sitting on the top of the side ridges. In the fully imbibed regime, the droplet never impacts on the top surface of the side ridges but falls into the scratch and spreads until an equilibrium is reached.

Finally, as shown in the 3D view included in bottom row of table 2, in the capillary regime, the droplet initially spills over onto the original substrate as in the quasi-spherical cap and inertial regimes. However, then the capillary flow forms and liquid spreads along the scratch by capillary action until there is no more fluid to supply further flow. This can be clearly seen in the evolution of both D_{Along} and the droplet height in figure 8b. Note the different scale on the time axis in this plot compared to the others in figure 8.

The rate of capillary propagation has been studied extensively starting with work by Washburn (1921), Bell & Cameron (1906) and Lucas (1918) who worked on cylindrical capillaries. The main finding was that propagation length x increases as the square root of time, that is $x \propto \sqrt{t}$. Other geometries have more recently been considered including rectangular channels. Relevant to the geometry considered here, capillary flow in open rectangular micro-channels has been studied theoretically and experimentally by Yang *et al.* (2011). They followed a similar approach to that used to derive the original Washburn model except that they applied the procedure to an open rectangular micro-channel. The reservoir droplet in their experiments was large enough relative to the micro-channel to ignore its Laplace pressure in the model. Although the capillary flow seen here initially follows this expected propagation rate, the very limited finite volume of the droplet supplying the flow soon results in a more rapid decrease in the speed of propagation and the corresponding flattening of the D_{Along} curve in figure 8b.

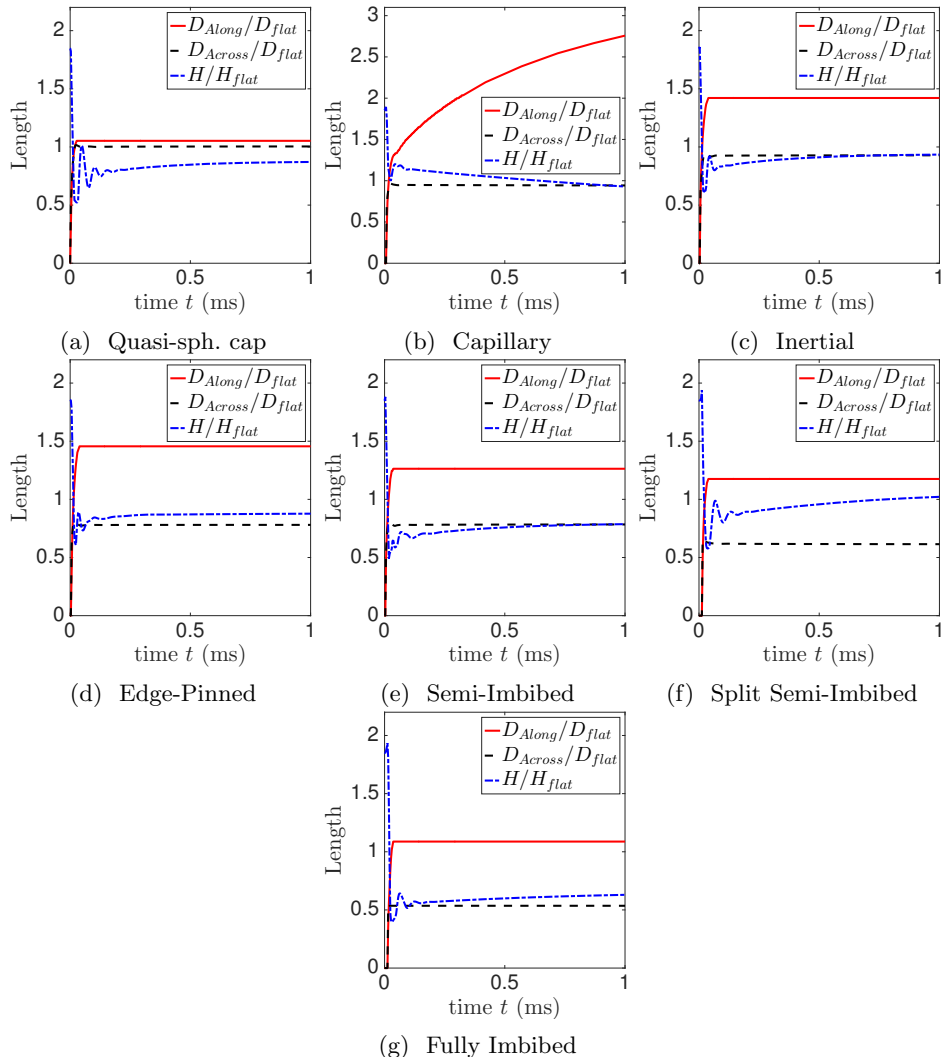


Figure 8: Evolution of the morphology dimensions with time for the various morphologies with corresponding widths and depths in table 2.

4.4. Groove without ridges

Removing the side ridges from the topography reduces the number of possible morphologies from seven to five, and alters the combinations of groove width and depth at which the morphologies arise. The corresponding regime map was constructed from simulations for groove widths ranging from 0.1–1 and depths of 0.05–0.75 with increments of 0.1 and 0.05 respectively, and the result is shown in figure 9. The morphologies caused by the presence of the ridges, namely edge-pinned and inertial (where the droplet spills over the ridges), are not seen with this topography; they both become identical to the semi-imbided morphology, where the equilibrium shape of the droplet occupies both the groove and the nearby region of the substrate surface. This is in fact the dominant morphology for sufficiently shallow grooves. For narrow and shallow grooves, the morphology can still be classed as a quasi-spherical cap, and for narrow and deep

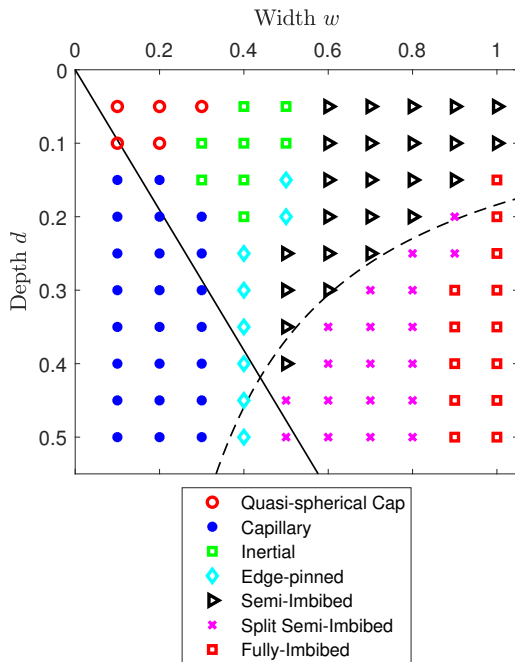


Figure 9: Regime map of equilibrium morphologies formed by printing a single droplet centred on a groove of width w and depth d with no side ridges for $Re = 204$ and $We = 26$.

grooves, the capillary morphology is still seen. The fully imbibed, and split semi-imbided morphologies are again seen for sufficiently wide and deep grooves.

4.5. Effect of Flow and Substrate parameters

The regime maps in figures 7 and 9 were constructed using a specific set of material and flow parameters θ_A , θ_R , Re , and We to illustrate the effects of the scratch geometry and the relationships among the morphologies. The following sub-sections discuss the influence of these parameters on the droplet behaviour when landing on a scratch with side ridges.

4.5.1. Effect of the advancing contact angle, θ_A

The advancing contact angle θ_A affects the spreading of droplets, as can be seen from equation (3.2). It also governs whether capillary flow will occur. To study this, simulations using $\theta_A = 75, 90, 115^\circ$, keeping $\theta_R = 1^\circ$, were run and the results plotted in figure 10 and tabulated oblique images in table 3. Note that the droplet dimensions along and across to the scratch, D_{Along} and D_{Across} respectively, are also normalised by D_{flat} , the equilibrium diameter of a corresponding droplet deposited on a smooth flat surface. Increasing θ_A will result in a decrease in both D_{Along} and D_{Across} as seen in figure 10 and table 3. This is because the capillary force due to wetting varies inversely with the contact angle and will assist wetting for $\theta_A < \pi/2$, hinder spreading for $\theta_A > \pi/2$, and not contribute to the force balance when $\theta_A = \pi/2$.

In the quasi-spherical cap regime, the small liquid volume that runs along the scratch decreases with increasing θ_A until it no longer extends beyond D_{flat} , and for higher θ_A the

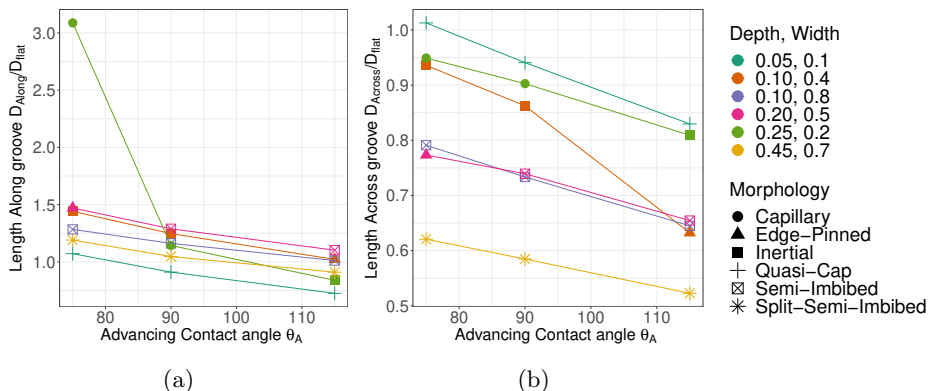


Figure 10: Effect of the θ_A on morphology dimensions for $Re = 204$, $We = 26$ and $\theta_R = 1^\circ$.

liquid inside the scratch does not extend as far as that above the scratch — see for example the $\theta_A = 115^\circ$ case in table 3. A similar effect is seen in the inertial morphology regime, but increasing θ_A sufficiently also stops the fluid from overspilling onto the original substrate, as seen for $\theta_A = 115^\circ$ in table 3; this transforms the morphology to the semi-imbided or edge-pinned. The capillary regime does not exist for $\theta_A \geq \pi/2$, as seen by the sharp decrease in D_{Along} in figure 10a for the case $d = 0.25$, $w = 0.2$ and the images in table 3; this transforms the morphologies into the inertial regime.

In the semi-imbided regime, increasing the advancing contact angle clearly changes the curvature of the contact line inside the scratch as well as causing the entire shape of the morphology to spread less in all directions. The same effect is seen for the split-semi-imbided regime. For groove dimensions that previously produced the edge-pinned morphology, increasing θ_A changes the curvature of the contact line inside the groove, and the contact line does not reach the outer edges of the side ridges for higher θ_A , hence moving into the semi-imbided morphology as seen in table 3. We conclude that the boundaries within the regime map in figure 7 shift towards lower widths as θ_A increases, with the capillary regime eventually disappearing.

4.5.2. Effect of Receding contact angle, θ_R

If, as the droplet shape changes, the contact angle falls below the receding contact angle, the contact line will recede. To illustrate the effect of θ_R , in the following results the advancing contact angle is fixed at $\theta_A = 75^\circ$ and θ_R has different values: $(1, 20, 35, 50, 75)^\circ$. Top views of the resulting equilibrium morphologies are in table 4 and equilibrium lengths along and across the morphology are in figure 11. For the quasi-spherical cap morphology, the footprint becomes thinner in the direction across the groove with increasing θ_R . This is because at sufficiently great θ_R , contact line pinning stops and the droplet recedes until an equilibrium is reached. This can be seen in figure 11b for $d = 0.05$, $w = 0.1$ where D_{Across} is the same for $\theta_R = 1^\circ$ and 20° and starts decreasing for greater θ_R due to the lack of contact line pinning. The contact line inside the groove stays pinned for values of θ_R up to 50° then starts receding as seen in figure 11a.

The inertial morphology decreases in D_{Along} and D_{Across} as seen in table 4 and figure 11 for $d = 0.1$, $w = 0.4$. The contact line starts receding starting from a moderate θ_R until it reaches a new equilibrium. The inertial morphology becomes edge-pinned and

Table 3: Effect of θ_A for $Re = 204$, $We = 26$ and $\theta_R = 1^\circ$.

θ_A	Quasi Cap $d = 0.05$ $w = 0.1$	Inertial $d = 0.10$ $w = 0.4$	Capillary $d = 0.25$ $w = 0.2$	Semi Imbided $d = 0.10$ $w = 0.8$	Split Semi Imbided $d = 0.45$ $w = 0.7$	Edge Pinned $d = 0.20$ $w = 0.5$	Fully Imbided $d = 0.50$ $w = 1.0$
θ_A 75°							
θ_A 90°							
θ_A 115°							

semi-imbided for θ_R values of 50° and 75° respectively because the contact line spills over then recedes and climbs back onto the side ridges. The liquid inside the groove also recedes with higher θ_R . In the capillary morphology, the length along the groove increases because more fluid is allowed to recede into the groove; for higher θ_R , the entire droplet volume ends up in the groove. The semi-imbided morphology turns into a fully imbided due to the recession of the footprint outside the groove into it, which explains the increase in D_{Along} . The edge-pinned morphology turns into a semi-imbided and then fully-imbided as θ_R approaches θ_A . This results in an increase in D_{Along} . The fully imbided morphology is not affected until $\theta_R = 75^\circ$ where its D_{Along} becomes shorter because the fluid recedes and satisfies the new receding contact angle. Increasing the receding contact angle generally results in an equilibrium morphology that is less spread in the direction perpendicular to the scratch, and also shorter in the direction along the scratch. The exceptions are the capillary and edge-pinned regimes, where the lack of contact-line pinning on the upper substrate releases more liquid to penetrate along the scratch. All the regimes shift to lower widths, except the capillary regime because it is governed by θ_A .

4.5.3. Effect of Reynolds number, Re

Increasing Reynolds number corresponds to increasing the impact inertia of the droplet, which results in greater spreading and hence increases in both D_{Along} and D_{Across} as seen in figure 12. This is true for all morphology types. Increasing Re shifts the boundary between the quasi-spherical cap and inertial regimes towards lower widths and depths because more spreading occurs along the scratch and hence more deviation from the spherical cap morphology. In addition, increasing Re will affect whether overspill will

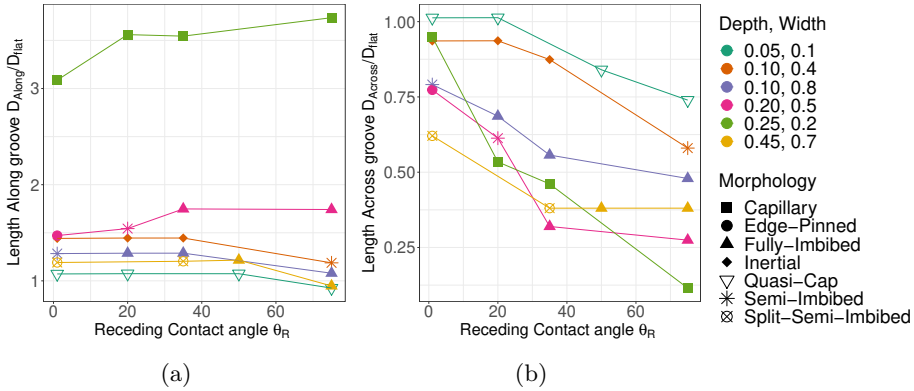


Figure 11: Effect of θ_R on morphology dimensions for $Re = 204$, $We = 26$ and $\theta_A = 75^\circ$.

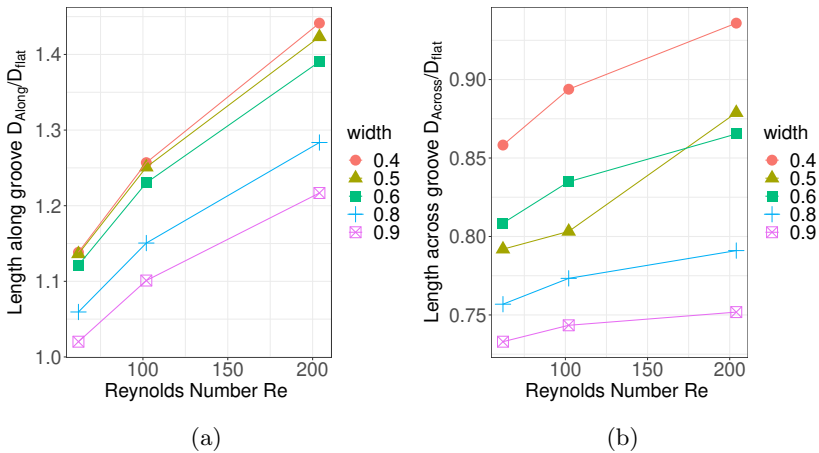


Figure 12: Effect of Re on morphology dimensions for $d = 0.15$, $We = 26$, $\theta_A = 75^\circ$ and $\theta_R = 1^\circ$.

occur and hence shifts the boundary between inertial or edge-pinned and semi-imbided morphologies towards larger widths. This can be seen in table 5 for $w = 0.5$ where for $Re = 62, 102$ the morphology is edge-pinned, but for $Re = 204$ overspill occurs, resulting in an inertial morphology and the corresponding sharp increase in D_{Across} seen in figure 12b. Hence achieving an edge-pinned morphology at this higher Reynolds number would require a wider scratch.

4.5.4. Effect of Weber number, We

Weber number is the ratio of inertial to interfacial energies, where higher surface tension corresponds to lower Weber numbers. For a wetting fluid, higher surface tension can assist in spreading, resulting in higher spreading lengths along and across the groove for lower We as seen in figure 13. This is consistent with equation (3.2), which for $\theta_A = 75^\circ$ and $Re = 204$ also predicts a decreasing trend in spreading diameter with increasing We . Other theoretical predictions that do not account for θ_A , such as that of

Table 4: Effect of θ_R for $\theta_A = 75^\circ$, $Re = 204$, and $We = 26$.

θ_R	Quasi Cap $w = 0.1$ $d = 0.05$	Inertial $w = 0.4$ $d = 0.10$	Capillary $w = 0.2$ $d = 0.25$	semi Imbibed $w = 0.8$ $d = 0.10$	split semi Imbibed $w = 0.7$ $d = 0.45$	Edge pinned $w = 0.5$ $d = 0.20$	Fully Imbibed $w = 1.0$ $d = 0.50$
θ_R 1°							
θ_R 20°							
θ_R 35°							
θ_R 50°							
θ_R 75°							

Roisman (2009),

$$\frac{D_{max}}{D_0} \approx 0.87Re^{1/5} - 0.4Re^{2/5}We^{-1/2} \quad (4.3)$$

predict the opposite behaviour, highlighting the importance of including the advancing contact angle, particularly for the small droplets considered here.

Decreasing We has a similar effect on the equilibrium morphology shifts as increasing Re . For example for $d = 0.2, w = 0.4$ as seen in table 6 the droplet is edge-pinned at $We = 60$ but as We is decreased, it spills over onto the original substrate, resulting in an inertial regime morphology. When $d = 0.25, w = 0.5$, the morphology is semi-imbibed for $We = 60$ but further spreading occurs, making it edge-pinned, as We is decreased to $We = 26$. There is a transition from semi-imbibed for $We = 60$ to edge-pinned for $We = 40$ and to inertial for $We = 26$.

Table 5: The effect of Re for some demonstrative simulations for $We = 26$, $\theta_A = 75^\circ$ and $\theta_R = 1^\circ$.

d	0.1	0.1	0.1	0.1	0.1	0.1	0.1	0.1	0.1	0.1
w	0.1	0.2	0.3	0.4	0.5	0.6	0.7	0.8	0.8	0.9
Re 62										
Re 102										
Re 204										

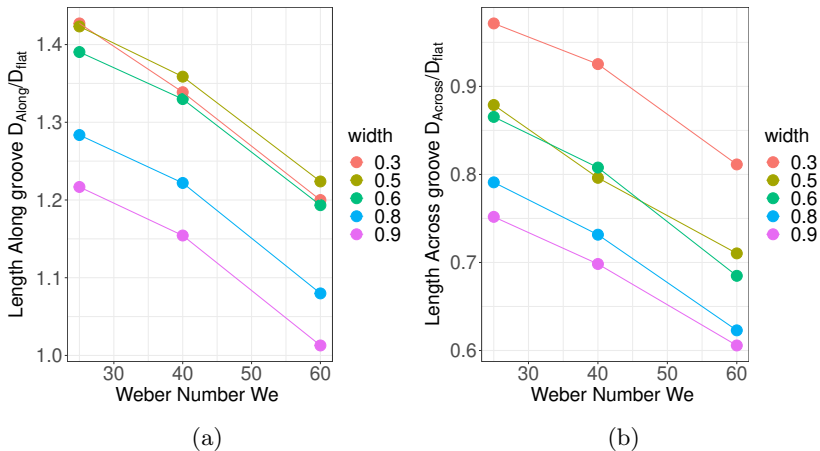


Figure 13: Effect of We on morphology dimensions for $d = 0.15$ and $Re = 204$.

5. Implications for printing applications

The ascertained morphologies can have significant consequences for printing applications especially when droplets reach commensurate length scales with surface topographies. The quasi-spherical morphology, where the scratch is very thin and shallow, will not have a significant effect on a printed morphology. The capillary morphology, however, can cause some issues for printing by lengthening the printed morphology significantly in one direction due to capillary flow of length more than $3D_{flat}$ as seen in figures 6b and 8b. If, for instance, two lines are being printed adjacently for a printed circuit, this

Table 6: The effect of We for some demonstrative simulations for $Re = 204$.

w	0.2	0.2	0.4	0.5	0.5	0.6	0.7	0.8	0.9
d	0.15	0.35	0.2	0.25	0.1	0.3	0.35	0.4	0.45
We 60									
We 40									
We 26									

lengthening can cause the two lines to connect unintentionally, resulting in a short circuit. Because of the slower time-scale of this capillary flow, as seen in figure 8a, this issue can be avoided using a fast enough curing mechanism (sub-millisecond) or by using a larger advancing contact angle. Similarly, this morphology can be exploited to connect two lines by designing such a feature and using a slowly evaporating ink.

The edge-pinned morphology is an example of how structured substrates can be exploited to print lines with sharp edges. To demonstrate this effect, five droplets are printed into a groove with depths of $0.3D_0$ and $0.45D_0$ and width $0.4D_0$ both corresponding to edge-pinned morphologies. The results are visualised in figures 14 and 15. In the first simulation, ($d = 0.3$ and $w = 0.4$), although the first droplet forms a sharp edge as expected, subsequent droplets spill over as seen in figure 14. This occurs because the precursor droplet inside the groove is in the spreading path of the subsequent droplet; this causes it to spill over. Increasing the depth to 0.45, however, allows more volume for droplet spreading inside the groove, so overspill does not occur and a sharp line is formed along the outer edges of the side ridges, as seen in figure 15. These two simulations demonstrate how challenging printing a sharp line can be.

In printing an electrical circuit, a key requirement is continuity of the printed track. If the track were to be printed across an accidental scratch, there is potential for the continuity to be broken if the scratch is of a certain dimension. As a demonstration, five droplets were printed across a scratch with dimensions in the split semi-imbibed regime with the centre of the third droplet aligned with the scratch centre. At a depth of 0.45 and width of 0.4, the third droplet, landing on the scratch centre, splits along the inner edges of the scratch, as expected — see figure 16. When the fourth droplet is printed, however, it pushes back on the pre-existing liquid on the substrate making the morphology coalesce and become continuous again, see figure 16c. Increasing the scratch width to 0.6 stops this “push-back” effect and a discontinuity in the line is produced, see figure 17.

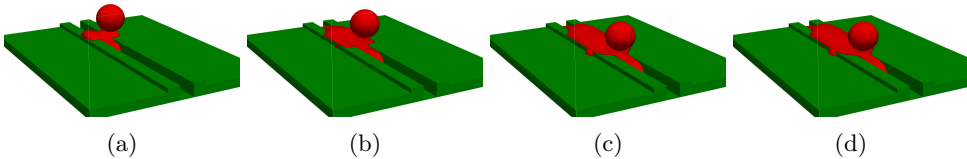


Figure 14: Printing five droplets along a scratch with depth $d = 0.3$ and width $w = 0.4$.

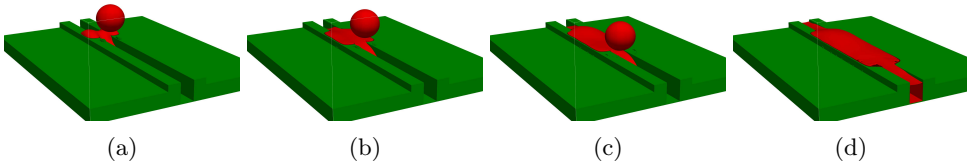


Figure 15: Printing five droplets along the scratch with depth $d = 0.3$ and width $w = 0.45$.

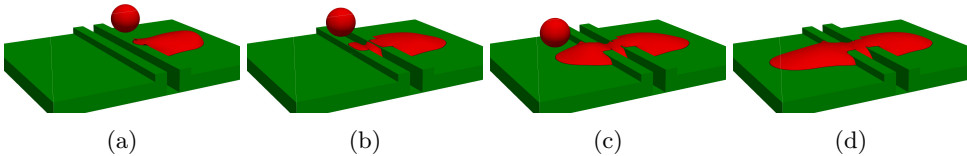


Figure 16: Printing across a scratch of depth $d = 0.4$ and width $w = 0.4$.

Similarly, the inertial and semi-imbibed morphologies, although not themselves split along edges, could cause a continuous line to split or deform due to the shortening of the spreading diameter across the scratch, and lengthening along it, as previously shown in figure 6. The split-semi-imbibed morphology will result in splitting of continuous morphologies. The simulations of printing along and across a scratch show that topographical features of commensurate size to droplets have a significant effect not only on a single droplet but also a series of droplets.

6. Conclusions

The printing of micro-droplets onto a scratched substrate has been investigated using a 3D multiphase lattice Boltzmann model implemented on a GPU architecture and validated against relevant previously published experiments. The scratch is idealised into a groove of rectangular cross-section, with rectangular side ridges representing material displaced from the groove. Seven distinct equilibrium morphologies are identified as a result of inertial spreading, contact line pinning on various features of the topography, imbibition of the droplet into the scratch and capillary flow along it. These morphologies arise for distinct ranges of scratch depth and width, relative to the droplet size, which define regions of a regime map that can be manipulated by varying the Reynolds number, Weber number, and advancing and receding contact angles.

From a practical perspective, the interaction of droplets with a scratch of commensurate size can be detrimental in different ways. When inkjet printing a track across a scratch, the shortening of the spreading in the direction perpendicular to the scratch means droplets may not join as intended, resulting in line breaks. Alternatively, for sufficiently deep and narrow scratches, capillary flow along the scratches could lead to unintentional connections between parallel tracks; in the case of printed electronics this

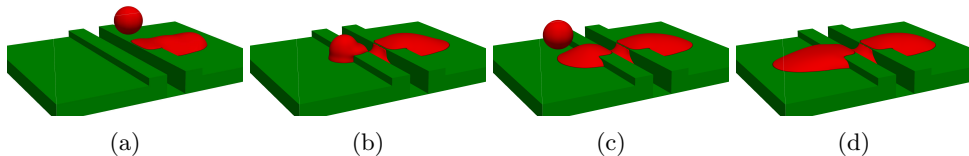


Figure 17: Printing across a scratch of depth $d = 0.4$ and width $w = 0.6$.

can result in malfunctioning circuits. However, this also suggests opportunity to exploit intentional features (such as those described by Nie & Kumacheva (2008), or Seemann *et al.* (2005)) to control spreading and maintain a uniform track on the substrate. As printing resolutions improve, and droplet sizes decrease, the results show that consideration of the substrate's topographical features becomes increasingly important in achieving desired printing outcomes.

Acknowledgements

The authors are grateful to the Engineering and Physical Sciences Research Council (EPSRC) Centre for Doctoral Training in Fluid Dynamics at the University of Leeds (Grant No. EP/L01615X/1) and Dupont Teijin Films (DTF) for financial support. Discussions with and insight from Andrew Bates and Kieran Looney from DTF were particularly useful; hence we sincerely thank them. We also thank the High Performance Computing facilities at the University of Leeds, where the simulations in this work were performed on machines ARC3 and ARC4.

Appendix A. Computational details

A.1. Discrete velocities

The discrete velocities used are the D3Q19 ones written as,

$$\mathbf{e}_i = \begin{bmatrix} 0 & 1 & -1 & 0 & 0 & 0 & 0 & 1 & -1 & 1 & -1 & 1 & -1 & 0 & 0 & 0 & 0 \\ 0 & 0 & 0 & 1 & -1 & 0 & 0 & 1 & -1 & -1 & 1 & 0 & 0 & 0 & 1 & -1 & 1 & -1 \\ 0 & 0 & 0 & 0 & 0 & 1 & -1 & 0 & 0 & 0 & 0 & 1 & -1 & -1 & 1 & 1 & -1 & -1 & 1 \end{bmatrix}$$

The source term used to incorporate the interaction force can be written as,

$$\mathbf{S} = \begin{bmatrix} 0 \\ F_x \\ F_y \\ F_z \\ 2\mathbf{F} \cdot \mathbf{u} + \frac{6\sigma|\mathbf{F}|^2}{\psi^2(s_\varepsilon^{-1}-0.5)} \\ 2(2F_x u_x - F_y u_y - F_z u_z) \\ 2(F_y u_y - F_z u_z) \\ F_x u_y + F_y u_x \\ F_x u_z + F_z u_x \\ F_y u_z + F_z u_y \\ c_s^2 F_y \\ c_s^2 F_x \\ c_s^2 F_z \\ c_s^2 F_x \\ c_s^2 F_z \\ c_s^2 F_y \\ 2c_s^2(u_x F_x + u_y F_y) \\ 2c_s^2(u_x F_x + u_z F_z) \\ 2c_s^2(u_y F_y + u_z F_z) \end{bmatrix}. \quad (\text{A } 1)$$

where \mathbf{F} is the total force with components F_x , F_y , and F_z .

A.2. Geometric Wetting Boundary Condition

Consider a droplet spreading on a solid surface with unit normal \mathbf{n} . The unit normal and unit tangent to the droplet surface are \mathbf{n}_s and \mathbf{t} respectively. Since the droplet is made of the liquid (heavy) phase submerged in the gas (light) phase, the density gradient at the droplet surface will point in the direction of $-\mathbf{n}_s$. Therefore,

$$\mathbf{n}_s = -\frac{\nabla\rho}{|\nabla\rho|}. \quad (\text{A } 2)$$

Looking at figure 18, an expression for θ is derived,

$$\tan\left(\frac{\pi}{2} - \theta\right) = \frac{\mathbf{n}_s \cdot \mathbf{n}}{|\mathbf{n}_s - (\mathbf{n}_s \cdot \mathbf{n})\mathbf{n}|}. \quad (\text{A } 3)$$

Substituting equation A 2 in A 3 and simplifying,

$$\tan\left(\frac{\pi}{2} - \theta\right) = \frac{-\nabla\rho \cdot \mathbf{n}}{|\nabla\rho - (\nabla\rho \cdot \mathbf{n})\mathbf{n}|}. \quad (\text{A } 4)$$

Equation (A 4) was discretised differently for the various parts of the geometry depending on the local normal \mathbf{n} . The geometry is illustrated through a cross-section seen in figure 19, with the various geometry types numbered. Similar boundary conditions are labelled with similar

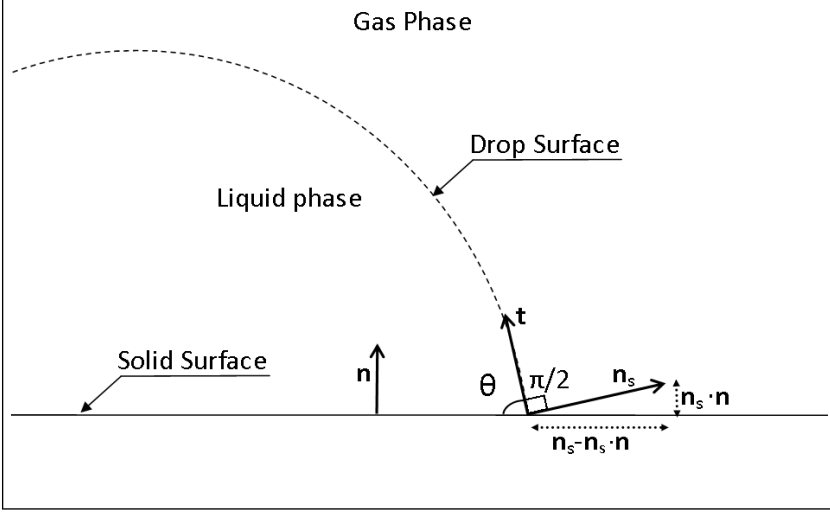


Figure 18: Schematic of the geometry at the three-phase contact line where \mathbf{n} is the unit normal to the solid surface, \mathbf{n}_s and \mathbf{t} are the unit normal and unit tangent to droplet surface. The unit normal to the fluid surface can be calculated using the density field which in turn can be used in geometric arguments to calculate the density on the solid surface to satisfy the contact angle θ .

patterns. The fluid domains are surrounded by ghost nodes whose density is calculated to satisfy a pre-determined contact angle. The density at these ghost cells of type 1 can be calculated using the equation (A 4), giving

$$\rho_{ijk} = \rho_{ij+2k} + \tan\left(\frac{\pi}{2} - \theta\right) \zeta, \quad (\text{A } 5)$$

where,

$$\zeta = \sqrt{(\rho_{i+1jk} - \rho_{i-1jk})^2 + (\rho_{ijk+1} - \rho_{ijk-1})^2}. \quad (\text{A } 6)$$

A similar form can be used for cell types 2,3, and 4. For corner 7,

$$\rho_{ijk} = \rho_{i+2j+2k} + \tan\left(\frac{\pi}{2} - \theta\right) \zeta, \quad (\text{A } 7)$$

where,

$$\zeta = \sqrt{(\rho_{i+1j+3k} - \rho_{i+3j+1k})^2 + 2(\rho_{i+2j+2k+1} - \rho_{i+2j+2k-1})^2}. \quad (\text{A } 8)$$

A similar form is used for all other corners. Equations (A 7) and (A 8) cannot be used for solid cells directly adjacent to corner cells because a solid cell might be used to update another solid cell. Instead, a second order accurate forward difference scheme is used for cell type 11,

$$\rho_{ijk} = \rho_{ij-2k} + \tan\left(\frac{\pi}{2} - \theta\right) \zeta, \quad (\text{A } 9)$$

where,

$$\zeta = \sqrt{(-\rho_{i+3j-1k} + 4\rho_{i+2j-1k})^2 - 3(\rho_{i+1j-1k+1} - \rho_{ij-1k-1})^2}. \quad (\text{A } 10)$$

A similar form was used for all solid cells neighbouring a corner.

A.3. Mesh Independence

To ensure sufficient resolution is used in simulations, results from increasingly finer lattices were compared to analytical predictions of the equilibrium diameter of a spreading droplet from equation (3.1). The error decreases gradually and matches the analytical curve seen in figure

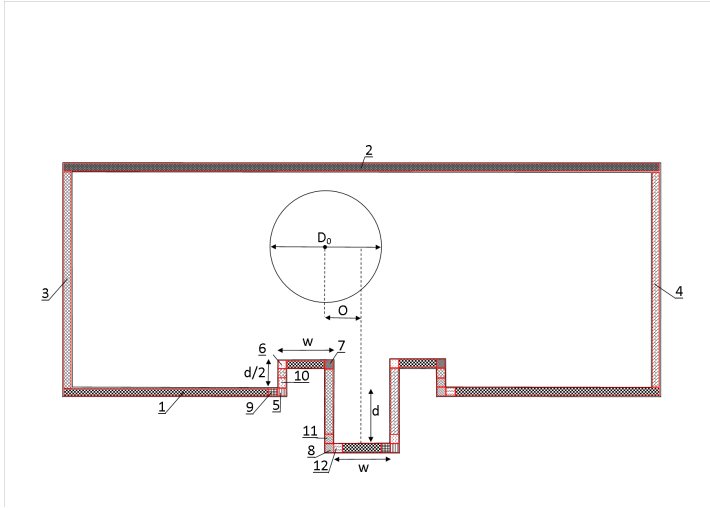


Figure 19: The fluid domain is surrounded by adjacent ghost lattice cells to apply the boundary conditions.

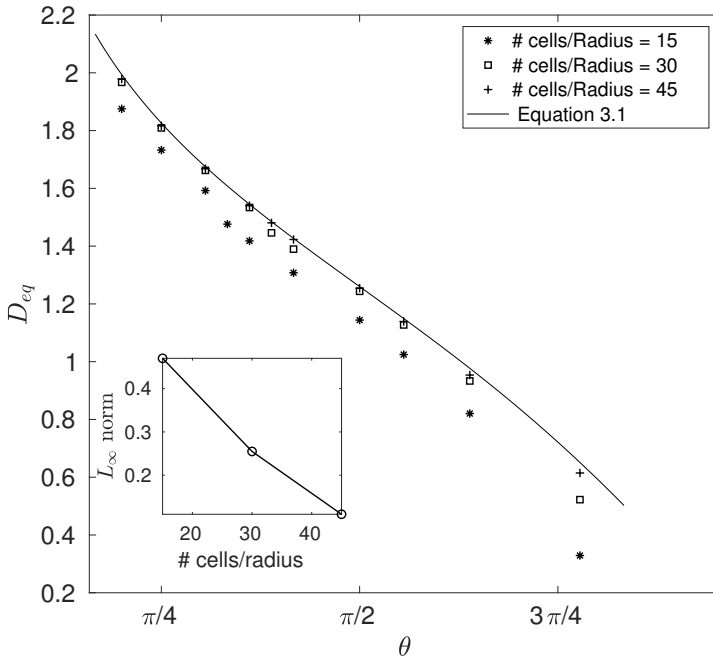


Figure 20: Comparison of simulation predictions with analytically derived D_{eq} values for different lattice resolutions.

20 for various angles with L_∞ error of approximately 0.1. The finest resolution was used in the simulations presented here.

REFERENCES

BELL, J. M. & CAMERON, F. K. 1906 The flow of liquids through capillary spaces. *The Journal of Physical Chemistry* **10** (8), 658–674.

- BUSSMANN, M., MOSTAGHIMI, J. & CHANDRA, S. 1999 On a three-dimensional volume tracking model of droplet impact. *Physics of Fluids* **11** (6), 1406–1417.
- CASTREJÓN-PITA, J. R., KUBIAK, K. J., CASTREJÓN-PITA, A. A., WILSON, M. C. T. & HUTCHINGS, I. M. 2013 Mixing and internal dynamics of droplets impacting and coalescing on a solid surface. *Phys. Rev. E* **88** (2), 023023.
- CHILTON, N. 2012 Printed Circuit Board Fabrication. In *Inkjet Technology for Digital Fabrication* (ed. Ian M. Hutchings & Graham D. Martin), chap. 8, pp. 183–206. Chichester, UK: John Wiley & Sons, Ltd.
- CONNINGTON, K. & LEE, T. 2013 Lattice boltzmann simulations of forced wetting transitions of drops on superhydrophobic surfaces. *Journal of Computational Physics* **250**, 601–615.
- VAN DAM, D. B. & LE CLERC, C. 2004 Experimental study of the impact of an ink-jet printed droplet on a solid substrate. *Physics of Fluids* **16** (9), 3403–3414.
- DAVIS, S. H. 1980 Moving contact lines and rivulet instabilities. part 1. the static rivulet. *Journal of Fluid Mechanics* **98** (2), 225–242.
- DE JONG, R., ENRÍQUEZ, O. R. & VAN DER MEER, D. 2015 Exploring droplet impact near a millimetre-sized hole: comparing a closed pit with an open-ended pore. *Journal of Fluid Mechanics* **772**, 427–444.
- D’HUMIÈRES, D., GINZBURG, I., KRAFCZYK, M., LALLEMAND, P. & LUO, L. S. 2002 Multiple-relaxation-time lattice Boltzmann models in three dimensions. In *Philosophical Transactions of the Royal Society A: Mathematical, Physical and Engineering Sciences*, , vol. 360, pp. 437–451.
- DING, H. & SPELT, P. D. M. 2007 Wetting condition in diffuse interface simulations of contact line motion. *Physical Review E - Statistical, Nonlinear, and Soft Matter Physics* **75** (4), 046708.
- DO, J., ZHANG, J. Y. & KLAPPERICH, C. M. 2011 Maskless writing of microfluidics: Rapid prototyping of 3d microfluidics using scratch on a polymer substrate. *Robotics and Computer-Integrated Manufacturing* **27** (2), 245–248.
- DUINEVELD, P. C. 2003 The stability of ink-jet printed lines of liquid with zero receding contact angle on a homogeneous substrate. *Journal of Fluid Mechanics* **477**, 175–200.
- GUNSTENSEN, A. K., ROTHMAN, D. H., ZALESKI, S. & ZANETTI, G. 1991 Lattice Boltzmann model of immiscible fluids. *Physical Review A* **43** (8), 4320–4327.
- HE, X., CHEN, S. & ZHANG, R. 1999 A lattice Boltzmann scheme for incompressible multiphase flow and its application in simulation of Rayleigh–Taylor instability. *Journal of Computational Physics* **152** (2), 642–663.
- HUANG, H., SUKOP, M. & LU, X. 2015 *Multiphase lattice Boltzmann methods: Theory and application*. Chichester, West Sussex, UK: John Wiley & Sons.
- JACKSON, F. F., KUBIAK, K. J., WILSON, M. C. T., MOLINARI, M. & STETSYUK, V. 2019 Droplet misalignment limit for inkjet printing into cavities on textured surfaces. *Langmuir* **35**, 9564–9571.
- JOSSERAND, C. & THORODDSEN, S. T. 2016 Drop impact on a solid surface. *Annual Review of Fluid Mechanics* **48** (1), 365–391.
- KANT, P., HAZEL, A. L., DOWLING, M., THOMPSON, A. B. & JUEL, A. 2017 Controlling droplet spreading with topography. *Phys. Rev. Fluids* **2**, 094002.
- KRÜGER, T., KUZMIN, A., KUSUMAATMAJA, H., SHARDT, O., SILVA, G. & VIGGEN, E. M. 2016 *The lattice boltzmann method: Principles and practice*. AG Switzerland: Springer International Publishing.
- KWON, J.-S., LEE, D. J. & OH, J. H. 2018 Formation and Characterization of Inkjet-Printed Nanosilver Lines on Plasma-Treated Glass Substrates. *Applied Sciences* **8** (2), 280.
- LI, Q., DU, D. H., FEI, L. L. & LUO, K. H. 2019 Three-dimensional non-orthogonal MRT pseudopotential lattice boltzmann model for multiphase flows. *Computers & Fluids* **186**, 128–140.
- LI, Q., LUO, K. H., KANG, Q. J. & CHEN, Q. 2014 Contact angles in the pseudopotential lattice Boltzmann modeling of wetting. *Physical Review E* **90** (5), 53301.
- LI, Q., LUO, K. H. & LI, X. J. 2013 Lattice boltzmann modeling of multiphase flows at large density ratio with an improved pseudopotential model. *Phys. Rev. E* **87** (5), 053301.
- LIM, T., HAN, S., CHUNG, J., CHUNG, J. T., KO, S. & GRIGOROPOULOS, C. P. 2009

- Experimental study on spreading and evaporation of inkjet printed pico-liter droplet on a heated substrate. *International Journal of Heat and Mass Transfer* **52** (1-2), 431–441.
- LUCAS, R. 1918 Ueber das zeitgesetz des kapillaren aufstiegs von flüssigkeiten. *Colloid & Polymer Science* **23** (1), 15–22.
- NIE, Z. & KUMACHEVA, E. 2008 Patterning surfaces with functional polymers. *Nature materials* **7** (4), 277–290.
- PASANDIDEH-FARD, M., QIAO, Y. M., CHANDRA, S. & MOSTAGHIMI, J. 1996 Capillary effects during droplet impact on a solid surface. *Physics of fluids* **8** (3), 650–659.
- RASHIDIAN, H., SELLIER, M. & MANDIN, P. 2019 Dynamic wetting of an occlusion after droplet impact. *International Journal of Multiphase Flow* **111**, 264–271.
- RIOBOO, R., MARENGO, M. & TROPEA, C. 2002 Time evolution of liquid drop impact onto solid, dry surfaces. *Experiments in Fluids* **33** (1), 112–124.
- ROISMAN, I. V. 2009 Inertia dominated drop collisions. II. An analytical solution of the Navier-Stokes equations for a spreading viscous film. *Physics of Fluids* **21**, 052104.
- SEEMANN, R., BRINKMANN, M., KRAMER, E. J., LANGE, F. F. & LIPOWSKY, R. 2005 Wetting morphologies at microstructured surfaces. *Proceedings of the National Academy of Sciences* **102** (6), 1848–1852.
- SHAN, X. & CHEN, H. 1993 Lattice Boltzmann model for simulating flows with multi phases and components. *Physical Review E* **47** (3), 1815–1819.
- SOLTMAN, D. B. 2011 Understanding inkjet printed pattern generation. PhD thesis, University of California at Berkeley.
- SWIFT, M. R., OSBORN, W. R. & YEOMANS, J. M. 1995 Lattice Boltzmann simulation of nonideal fluids. *Physical Review Letters* **75** (5), 830–833.
- WASHBURN, E. W. 1921 The dynamics of capillary flow. *Physical review* **17** (3), 273.
- WILSON, M. C. T. & KUBIAK, K. J. 2016 Simulation of drops on surfaces. In *Fundamentals of Inkjet Printing* (ed. Stephen D Hoath), chap. 11, pp. 281–312. Weinheim, Germany: Wiley-VCH.
- YANG, D., KRASOWSKA, M., PRIEST, C., POPESCU, M. N. & RALSTON, J. 2011 Dynamics of capillary-driven flow in open microchannels. *The Journal of Physical Chemistry C* **115** (38), 18761–18769.
- YUAN, P. & SCHAEFER, L. 2006 Equations of state in a lattice Boltzmann model. *Physics of Fluids* **18** (4), 3452.
- ZHANG, L., CHENG, X., KU, T., SONG, Y. & ZHANG, D. 2018 Lattice boltzmann study of successive droplets impingement on the non-ideal recessed microchannel for high-resolution features. *International Journal of Heat and Mass Transfer* **120**, 1085–1100.